PCCP

Accepted Manuscript

ROYAL SOCIETY OF CHEMISTRY

www.rsc.org/pccp

Perfect inhibition of CdS photocorrosion by graphene sheltering engineering on TiO_2 nanotube array for highly stable photocatalytic activity

Yanhong Tang [a,*], Xu Hu [a], Chengbin Liu [b,*]

[a] *College of Materials Science and Engineering, Hunan University, Changsha 410082, P. R. China*

[b] *State Key Laboratory of Chemo/Biosensing and Chemometrics, Hunan University, Changsha 410082, P. R. China*

Corresponding authors

Tel.: +86-731-88823805

E-mail address: tangyh@hnu.edu.cn (Y. Tang); chem_cbliu@hnu.edu.cn (C. Liu)

ABSTRACT

An artful graphene sheltering engineering onto TiO_2 nanotube array for perfect inhibition of CdS photocorrosion (RGO/CdS–TiO_2 NT) has been developed by one-step electrodeposition method. The CdS photocorrosion driven by both holes and radicals has been systematically investigated and identified. The RGO layer provides a perfect protection to CdS through (i) blocking the attack of active species especially •OH radicals and (ii) offering a closed electron-rich microenvironment where the stored electrons RGO(e^-) not only reduce intermediate species $S^{\bullet -}$ to S^{2-} but also compensate the valence band of CdS for its loss of electrons to alleviate CdS photocorrosion from oxidation by holes. The photocatalyst exhibits extremely high stability. RGO/CdS–TiO_2 NT shows high visible-light photocatalytic activity for the degradations of organic dye methylene blue (MB), industrial chemical p-nitrophenol (PNP) and herbicide 2,4–dichlorophenoxyacetic acid (2,4–D). This work provides a new insight into the protection of photosensitive semiconductors from photocorrosion.

1. Introduction

As a visible-light-driven photocatalyst, cadmium sulfide (CdS) has been extensively investigated. However, the core problem is still related to its photocorrosion. It greatly obstructs its practical application due to loss of activity and cadmium leakage pollution. Therefore, many efforts have been done to restraint the photochemical instability of CdS by introducing sacrificial reagents [1], coupling CdS with wide-bandgap semiconductor [2,3] or oxidation co-catalyst [4], and constructing a core-shell heterostructure [5,6]. Commonly, people have charged the photocorrosion to the factor that the sulfide ion is highly prone to oxidation by photogenerated holes [7]. In fact, other active species, especially hydroxyl radicals (•OH), may be also involved in the oxidation of sulfur [8]. However, these factors are neglected in the theoretical analysis. These active species are strong enough to oxidize sulfide ion and the exposure of CdS to these active species is still fatal [9]. It is therefore absolutely vital to develop suitable interface engineering methods to satisfy the inhibition of CdS photocorrosion from the oxidation by both photogenerated holes and active radicals. Constructing a shield between CdS and active radicals seems a feasible way to inhibiting the photocorrosion from the attack of active radicals. However, the shield may not only reduce the inherent optical absorption of CdS but also block the transfer

of photogenerated charges to the interface between photocatalyst and reaction medium. Therefore, developing a suitable sheltering engineering between CdS and shield is very challenging.

We demonstrate herein one-step co-electrodeposition of CdS nanoparticles and reduced graphene oxide (RGO) film onto TiO_2 nanotube array (RGO/CdS–TiO_2 NT) where CdS nanoparticles are well blanketed with a thin layer of RGO film (Scheme 1). Although graphene has been used in anti-photocorrosion of photosensitive semiconductors, the synthetical affection of active species including radicals on photocorrosion are neglected [10-12]. The factors on photocorrosion of CdS have been herein systematically investigated and CdS photocorrosion driven by both h^+ and •OH radicals has been identified. The RGO sheltering engineering effectively inhibits the photocorrosion from hole and active radical-induced oxidation. The photocatalytic performance of RGO/CdS–TiO_2 NT is evaluated by the photocatalytic degradation of typical organic pollutants.

2. Experimental

2.1. Materials

Titanium foil (99.8%, 250 μm thickness) was purchased from Aldrich (Milwaukee, WI), graphite powder about 50 μm was purchased from Shanghai

Carbon Co., Ltd., and other reagents are of analytical grade and used as received. Deionized water was used for preparation of all aqueous solutions.

2.2. Fabrication of RGO/CdS–TiO_2 NT

The TiO_2 NT was prepared by the method of anode oxidation. Typically, prior to anodization, titanium foils were ultrasonically cleaned in acetone and ethanol, respectively. The anodizing cell was a two–electrode system using platinum as the counter electrode. The cleaned foil was anodized at 15 V in an electrolyte containing 0.1 M NaF and 0.5 M $NaHSO_4$ at room temperature for 3 h. The efficient electrode area is 4 cm × 1 cm. The as-anodized TiO_2 NT was sintered in oxygen atmosphere at 500ºC for 3 h with heating and cooling rates of 2ºC·min^{-1} to obtain photoactive anatase phase. Reduced graphene oxide (RGO) and CdS were co-deposited onto TiO_2 NT by cyclic voltammetric electrodeposition. Typically, the as–prepared graphite oxide from a modified Hummers method was ultrasonically exfoliated in 0.1 M citrate buffer solution of pH 4.0 for 3 h to form a homogeneous electrolyte A (graphene oxide, GO). $CdCl_2$ and $Na_2S_2O_3$ were dissolved in a 0.1 M citrate buffer solution of pH 4.0 to form electrolyte B. The precursor electrolyte was prepared by mixing A and electrolyte B with a concentration of 0.3 mg·mL^{-1}, 0.06 M and 0.1 M for GO, $CdCl_2$ and $Na_2S_2O_3$, respectively. The cyclic voltammetric reduction was performed in the

precursor electrolyte, using a three–electrode configuration with the annealed TiO_2 NT/Ti sheet as the working electrode, a Pt foil as the counter electrode, and a saturated calomel electrode (SCE) as the reference electrode on a CHI 660D electrochemical workstation (Chenhua, Shanghai, China). The scan was from –1.5 to 0.6 V with a rate of 25 $mV \cdot s^{-1}$. After deposition, the working electrode was washed with deionized water, getting RGO/CdS–TiO_2 NT hybrid. As a control, RGO–TiO_2 NT was prepared by only using electrolyte A (0.3 $mg \cdot mL^{-1}$ GO) with a scan rate of 50 mV s^{-1} from –1.5 to 1 V and CdS–TiO_2 NT was prepared by using electrolyte B (0.06 M $CdCl_2$ and 0.1 M $Na_2S_2O_3$) with a scan rate of 25 mV s^{-1} from –1.5 to 0.6 V. The loading of graphene or CdS was controlled by the number of potential cycles.

2.3. Structure characterization

The morphologies of the hybrids were characterized by a field emission scanning electron microscope (FESEM, Hitachi S−4800, Japan) and a transmission electron microscope (TEM, JEOL JEM-2100F, Japan). Energy dispersive X–ray (EDX) spectrometer fitted to the electron microscope was applied for elemental analysis. The crystal phases of the hybrids were determined by an X–ray diffractometer with Cu−K_α radiation (XRD, M21X, MAC Science Ltd., Japan). The binding energies of S, Cd and C of the composites were determined by X-ray photoelectron spectroscopy

(XPS, K-Alpha 1063, Thermo Fisher Scientific, England) with an Al−K_α X-ray source.

2.4. Property measurement

The UV–vis diffuse reflectance spectra (DRS) were recorded with a UV–visible spectrophotometer (Cary 300, USA) equipped with an integrating sphere with the radius of 150 mm. The photocurrents were recorded on the CHI 660D electrochemical workstation by using a three−electrode configuration with bare TiO_2 NT or the modified TiO_2 NT/Ti sheet as the working electrode, Pt foil as the counter electrode and an SCE as the reference electrode in 0.5 M Na_2SO_4 solution. A 500 W xenon arc lamp with a 420 nm optical filter (CHF−XQ−500W, Beijing Changtuo Co., Ltd.) served as visible light source with the photon flux of 100 $mW \cdot cm^{-2}$ measured by NOVA Oriel 70260 with a thermodetector. The temperature-programmed oxidation (TPO) experiments were carried out on AutoChem II 2920 (Micromeritics, USA) at a ramping rate of 10 K/min in mixed helium and oxygen flow.

2.5. Evaluation of photocatalytic performance

Three typical organic pollutants were chosen in terms of quantities used and potential environmental impacts: Organic dye methylene blue (MB), industrial chemical p-nitrophenol (PNP) and herbicide 2,4–dichlorophenoxyacetic acid (2,4–D).

The photocatalytic degradation experiments were carried out under stirring in a quartz beaker containing 50 mL 10 $mg \cdot L^{-1}$ MB, PNP or 2,4-D. The photocatalyst samples with a total active area of 8.0 cm^2 were vertically placed in the quartz beaker. A 500 W xenon arc lamp with a UV-cutoff filter ≥ 420 nm and the photon flux of 100 $mW \cdot cm^{-2}$ (CHF–XQ–500W, Beijing Changtuo Co. Ltd., China) served as a visible light source. Before irradiation, the system was maintained in the dark for 0.5 h to reach complete adsorption–desorption equilibrium, so that the decreased concentration of pollutants with irradiation time can fully reflect the photocatalytic activities of the catalysts. The real-time concentration of pollutants was determined by UV−vis spectrophotometry at the characteristic absorbance of 664 nm for MB, 317 nm for PNP or 227 nm for 2,4-D in a spectrophotometer (Cary 300, Varian, USA). The accurate concentrations of pollutants were determined by high–performance liquid chromatography (HPLC, Agilent 1100HPLC, USA).

2.6. Photocorrosion test

The photocorrosion on CdS–TiO_2 NT and RGO/CdS–TiO_2 NT under visible light irradiation was evaluated by the amount of Cd leakage which was determined by an inductively coupled plasma emission spectroscopy (ICP, 5300DV, PerkinElmer, USA). Additionally, the structures and morphologies of CdS–TiO_2 NT and

RGO/CdS–TiO_2 NT during photocorrosion test were determined by FESEM. In order to investigate the effect of active species on photocorrosion, herein, *t*BuOH was used to eliminate •OH radicals, EDTA-2Na was used to remove h^+, and N_2 was injected to clear out oxygen. The •OH radicals produced on CdS–TiO_2 NT and RGO/CdS–TiO_2 NT under visible-light irradiation were measured by the fluorescence method using terephthalic acid (TA) as a probe molecule (•OH + TA → TAOH). The fluorescence signals of TAOH were measured on a fluorescence spectrophotometer (Hitachi F-7000, Japan). The photoluminescence (PL) intensity of TAOH at 425 nm excited by 315 nm light was measured every 10 minutes.

3. Results and discussion

3.1. Characterization

Fig. 1 shows the SEM images of bare TiO_2 NT, CdS–TiO_2 NT, RGO–TiO_2 NT, and RGO/CdS(x)–TiO_2 NT, where x is the number of deposition cycle. Bare TiO_2 NT possesses a uniform tubular structure in pore size of 90 nm (Fig. 1a). The size of CdS nanoparticles in CdS–TiO_2 NT is about 50 nm (Fig. 1b). The RGO film layer forms in RGO–TiO_2 NT (Fig. 1c). The amount of CdS nanoparticles in RGO/CdS–TiO_2 NT increases with increasing deposition cycle but the size of CdS nanoparticles keep 30-50 nm (Fig. 1d-f). The RGO layer also becomes thicker with increasing potential

cycle. It is worthwhile to note that the CdS nanoparticles are compactly covered with RGO film layer. The vertical view of TEM image of RGO/$CdS_{(5)}$–TiO_2 NT clearly displays the spherical morphology of CdS nanoparticles in size of 30-50 nm (Fig. 1g). The energy dispersive X-ray (EDX) spectroscopy analysis (Fig. 1h) exhibits the characteristic peaks of C, O, S, Ti and Cd with the atom contents of 2.53% C, 0.2% Cd and 0.19% S. The nearly 1:1 molar ratio of Cd to S indicates the existence of CdS. Based on the photocurrent measurement of RGO/CdS(x)–TiO_2 NT (x= 5, 7, 10), RGO/$CdS_{(5)}$–TiO_2 NT shows the highest photocurrent density (Fig. 2). This could be explained by the facts: 1) the shadowing effect of the thicker RGO layer probably reduces the transmission of light to semiconductor, resulting in less photogenerated electrons; 2) the aggregation of more CdS nanoparticles is unfavorable for the transfer and separation of photoinduced carriers [13, 14]. Unless otherwise specified, RGO/CdS–TiO_2 NT only represents RGO/$CdS_{(5)}$–TiO_2 NT.

XRD characterization is an effective method to determine the crystal phase of materials. The XRD patterns in Fig. 3A reveal that all the samples display diffraction peaks indicative of anatase TiO_2 (JCPDS 21-1272) and wurtzite CdS (JCPDS 41-1049). Compared with other crystal phases, these crystal phases have been found to favor higher photocatalytic activity [15]. However, there is no characteristic peak of

C in the XRD pattern of RGO/CdS–TiO_2 NT, probably due to the amorphous state of graphene or its low crystal content resulting in low diffraction intensity [16].

Temperature-programmed oxidation (TPO) measurement can evaluate the chemical stability of materials. Fig. 3B shows the TPO curves of CdS, CdS–TiO_2 NT and RGO/CdS–TiO_2 NT. It displays that the oxidation of S^{2-} in CdS–TiO_2 NT occurs at 845K slightly higher than that in pure CdS (834K). In contrast, RGO/CdS–TiO_2 NT exhibits a higher oxidation temperature around 906K. The high oxidation temperature for RGO/CdS–TiO_2 NT reveals a strong interaction between CdS and RGO, inhibiting the oxidation of CdS.

The results of XPS spectra are shown in Fig. 4. Compared with the binding energies (BEs) of both S 2p and Cd 3d in pure CdS, those in CdS-TiO_2 NT increase slightly while those in RGO/CdS–TiO_2 NT increase significantly (Fig. 4B and C). The shift of binding energies in RGO/CdS–TiO_2 NT can be attributed to the strong interactions between CdS nanoparticles and RGO sheets [17,18]. The results are well consistent with the results of TPO analysis (Fig. 3B). The XPS spectrum of C 1s reveals that the peaks of C-O at 286.5 eV and C=O at 288.6 eV in GO (graphene oxide) nearly disappear after electrodeposition of GO onto TiO_2 NT (Fig. 4D), implying that the oxygen-containing functional groups in GO have been reduced

during electrochemical deposition process, resulting in RGO (reduce graphene oxide) [19]. When simultaneously depositing CdS and RGO onto TiO_2 NT, the peak at 288.6 eV increases again due to the formation of S-C bond resulting in higher binding energy of C 1s [20] which further confirms the strong interaction between RGO and CdS.

3.2. Photoelectrochemical property

The UV-vis diffuse reflectance spectroscopy (DRS) is commonly employed to characterize the absorption property of the materials. Among the samples, RGO/CdS–TiO_2 NT exhibits the strongest visible–light absorption attributed to the combined action of CdS and RGO (Fig. 5A). Obviously, the coating of transparent RGO layer does not impede the inherent optical absorption of CdS. The boosted absorption of light for RGO/CdS–TiO_2 NT in the visible light region can enhance the photoexcitation efficiency which is approved by photocurrent response where RGO/CdS–TiO_2 NT displays the highest photocurrent density (Fig. 5B). The high photocurrent density of RGO/CdS–TiO_2 NT should attribute to the fact that graphene has a strong ability in capturing and transporting photogenerated electrons from semiconductor [21]. The intimate contact between RGO and CdS is also crucial for the charge transport from CdS to RGO. It is worthwhile to note that under irradiation,

the photocurrent of CdS–TiO_2 NT gradually decreases while that of RGO/CdS–TiO_2 NT shows a stable trend. This strongly indicates that the RGO shield would highly strengthens the resistance to CdS photocorrosion.

3.3. Photocatalytic performance

Cadmium sulfide, one of the most technologically important semiconductor materials, has applications in a wide range of fields including photovoltaics [17], optoelectronics [18], chemical sensors [22], and photocatalysis [23]. As one of its application fields, the photocatalytic performances of the photocatalysts are evaluated for the degradation of organic dye methylene blue (MB) , industrial chemical p-nitrophenol (PNP) and herbicide 2,4–dichlorophenoxyacetic acid (2,4–D). For the selected pollutants, conventional wastewater treatment methods are gradually becoming inadequate to meet the requirements of a higher environmental quality [24].

Adsorptivity of catalysts towards pollutant molecules is a crucial factor required for efficient degradation. For convenient viewing of color change, MB was chosen as model pollutant for the adsorption experiment. All graphene modified TiO_2 NT hybrids, including RGO–TiO_2 NT and RGO/CdS–TiO_2 NT show higher adsorption amount of MB than bare TiO_2 NT and CdS–TiO_2 NT (Fig. 6A), due to the high

specific surface area of graphene nanosheets and their good affinity toward organic molecules through hydrophobic or specific π–π interactions [25].

The visible light photocatalytic degradation efficiencies of MB over the hybrids are shown in Fig. 6B. Obviously, MB is very stable in the absence of a photocatalyst (direct photolysis). After 100–min irradiation, CdS–TiO_2 NT and RGO/CdS–TiO_2 NT show 83% and nearly 100% decomposition efficiency of MB, respectively. In contrast, the photocatalysts without CdS (bare TiO_2 NT and RGO–TiO_2 NT) exhibit low decomposition efficiency of MB due to their poor absorption in visible light region. The degradation efficiencies of MB over the photocatalysts with RGO are higher than those over the photocatalysts without RGO (RGO–TiO_2 NT *vs* bare TiO_2 NT and RGO/CdS–TiO_2 NT *vs* CdS–TiO_2 NT), which is presumably benefited from the high charge separation (Fig. 5B) and adsorption capacity of RGO (Fig. 6A). Undoubtedly, the highest photocatalytic degradation efficiency of MB over RGO/CdS–TiO_2 NT should be attributed to the synergetic effect between RGO and CdS.

Kinetic constant can clearly reflect the decomposition rate of pollutants over photocatalysts. High decomposition rate is very significant for practical applications. The decomposition kinetics of MB under visible light irradiation follows essentially a first order kinetics, with classical equation $\ln(C/C_0) = k \cdot t$, where k is pseudo–first rate

kinetic constant and t is time (Fig. 6C). It demonstrates that under visible light irradiation the MB photodegradation rate over RGO/CdS–TiO_2 NT ($k = 0.03968\ min^{-1}$) is about 165, 104, and 1.7 times that over bare TiO_2 NT ($k = 0.00024\ min^{-1}$), RGO–TiO_2 NT ($k = 0.00038\ min^{-1}$), and CdS–TiO_2 NT ($k = 0.02279\ min^{-1}$), respectively. The results clearly show that RGO/CdS–TiO_2 NT is a highly effective visible light photocatalyst.

Good longevity is very important for practical application of photocatalysts. CdS has been widely used as photoelectric material while its poor stability blocks its further application. Herein, the longevities of the photocatalysts are investigated by recycling the photocatalysts for MB photocatalytic degradation under visible-light irradiation. As shown in Fig. 6D, CdS–TiO_2 NT almost completely loses photocatalytic activity after 2000-min visible-light irradiation, which should be mainly caused by serious photocorrosion of CdS. On the contrary, after even 3600-min visible-light irradiation, there is only an insignificant loss in the photocatalytic activity of RGO/CdS–TiO_2 NT, which might be partly caused by loss of CdS during each round of collection and rinsing. The excellent recycling performance and longevity of RGO/CdS–TiO_2 NT makes it a qualified candidate in practical applications.

In order to furthermore evaluate the photocatalytic property of RGO/CdS–TiO_2 NT photocatalyst, the photocatalytic degradations of PNP and 2,4-D over RGO/CdS–TiO_2 NT under visible-light irradiation are investigated (Fig. 7). After 0.5 h immersion in the dark to reach complete adsorption–desorption equilibrium, about 10% PNP or 2,4-D are adsorbed onto RGO/CdS–TiO_2 NT. Although PNP and 2,4-D are intractable due to their highly chemical stability, the photocatalytic decomposition efficiencies of them over RGO/CdS–TiO_2 NT still achieve nearly 100% after 140-min visible light irradiation.

3.4. Photocatalytic mechanisms

The photocatalytic mechanism of RGO/CdS–TiO_2 NT is shown as Scheme 2. Under visible light irradiation, the electrons of CdS are excited from the valence band (VB) to the conduction band (CB). The CB electrons of CdS can transfer to the CB of TiO_2 and then to RGO. Meanwhile, the CB electrons of CdS can directly transfer to RGO. Thus, the exciton recombination is highly suppressed in the ternary RGO/CdS–TiO_2 NT photocatalyst. During the photocatalysis process, the accumulated electrons in RGO will react with surface adsorbed oxygen molecules or dissolved oxygen in water to form $O_2\bullet^-$ superoxide ion radical. The $O_2\bullet^-$ superoxide ion radicals can directly attack organics or combine with protons (H^+) to generate

oxidative H_2O_2 and hydroxyl radicals (•OH). One the other hand, the holes may react with OH^- ions (or H_2O) to form •OH free radicals. The thus produced strongly oxidative •OH radicals along with the generated holes will attack organic pollutant molecules.

3.5. Photocorrosion tests

For photocorrosion tests, *t*BuOH was used to eliminate •OH radicals, EDTA-2Na was used to remove h^+, and N_2 was injected to clear out oxygen which could capture photogenerated electrons to form •OH radicals. The hydroxyl radicals (•OH) produced from CdS–TiO_2 NT and RGO/CdS–TiO_2 NT under visible-light irradiation were measured by the fluorescence method using terephthalic acid (TA) as a probe molecule (•OH + TA → TAOH) [26]. In the absence of any scavengers, the PL intensities of TAOH at 425 nm on both CdS–TiO_2 NT and RGO/CdS–TiO_2 NT steadily increase with prolonging irradiation time, revealing that more and more •OH radicals produce with increasing irradiation time (Fig. 8).

The results of photocorrosion tests on CdS–TiO_2 NT and RGO/CdS–TiO_2 NT under visible light irradiation are shown in Fig. 9. After 2000-min visible light irradiation in the presence of EDTA-2Na and N_2 without formation of h^+ and •OH radicals, both CdS–TiO_2 NT and RGO/CdS–TiO_2 NT keep intact structures and

morphologies (Fig. 9a1 and b1), accompanying with no leaching of Cd^{2+} (Fig. 9 c1). After 2000-min irradiation in the presence of only EDTA-2Na used to remove h^+, the photocorrosion of CdS–TiO_2 NT occurs, where the CdS particles become smaller and even disappear with significant leaching of Cd^{2+} (Fig. 9a2 and c2). In contrast, the CdS in RGO/CdS–TiO_2 NT is still stable with undetectable leaching of Cd^{2+} (Fig. 9b2 and c2). Undoubtedly, the S^{2-} in CdS–TiO_2 NT is highly prone to oxidation by photogenerated •OH radicals while the S^{2-} in RGO/CdS–TiO_2 NT survives due to the safeguard of RGO shield. After 2000-min irradiation in the presence of only *t*BuOH used to remove •OH radicals, the photocorrosion of CdS–TiO_2 NT also occurs with obvious leaching of Cd^{2+} due to the oxidation of h^+ (Fig. 9a3 and c3) while RGO/CdS–TiO_2 NT maintains intact structure and morphology with negligible leaching of Cd^{2+} (Fig. 9b3 and c3). Thus it can be seen that the RGO shield can effectively restrain the h^+-induced photocorrosion of CdS in RGO/CdS–TiO_2 NT. After 2000-min irradiation in the absence of scavengers and N_2, the photocorrosion significantly occurs on CdS–TiO_2 NT leaving tiny particles with serious leaching of Cd^{2+} (Fig. 9a4 and c4) due to the double attack from h^+ and •OH radicals while the CdS nanoparticles in RGO/CdS–TiO_2 NT are still tightly sheltered by RGO blanket with undetectable Cd^{2+} leakage (Fig. 9b4 and c4).

The results clearly present that both h^+ and •OH radicals but not only h^+ are responsible for photocorrosion of CdS and the RGO shield effectively inhibits the photocorrosion of CdS in RGO/CdS–TiO_2 NT. The photocorrosion inhibition mechanism is schematically illustrated as Scheme 3. The RGO layer not only significantly inhibits the photocorrosion of CdS from oxidation by active species especially •OH radicals through blocking the contact between these active species and CdS nanoparticles, but also provides a closed electron-rich microenvironment where the stored electrons RGO(e^-) can react with intermediate species S•$^-$ to regenerate S^{2-} [27]. Furthermore, the dissolution of CdS sheltered in a closed RGO blanket can be effectively restrained whereas the unbridled diffusion of S^{2-} into solution accelerates the dissolution of CdS in CdS–TiO_2 NT. In terms of the ambipolar charge transport [28] and heterogeneous electron transfer in graphene [29,30], the stored electrons RGO(e^-) serve as electron donors which can compensate the valence band of CdS for its loss of electrons, effectively alleviating the photocorrosion of CdS from oxidation by holes.

4. Conclusions

Perfect inhibition of CdS photocorrosion has been successfully achieved by RGO sheltering engineering built from one-step electrodeposition. The photocorrosion of

CdS by the oxidation of both h^+ and •OH radicals has been identified. The synergistic effect among CdS, RGO and TiO_2 NT guarantees excellent photocatalytic activity and photochemical stability of RGO/CdS–TiO_2 NT photocatalyst. The present result is therefore very encouraging and is expected to be a new strategy to enhance the photochemical stability of photosensitive semiconductors. Better understanding such high photochemical stability would give further hints for the design and assembly of more efficient photocatalytic systems.

Acknowledgments

This work was supported by Hunan Provincial Natural Science Foundation of China (14JJ1015), the National Natural Science Foundation of China (51178173, 51478171 and 51202065), Program for Innovation Research Team in University (IRT1238), and Program for New Century Excellent Talents in University (11-0126).

References

[1] Q. Li, B. Guo, J. Yu, J. Ran, B. Zhang, H. Yan, J. R. Gong, *J. Am. Chem. Soc.*, 2011, **133**, 10878−10884.

[2] L. Huang, X.L. Wang, J.H. Yang, G. Liu, J.F. Han, C. Li, *J. Phys. Chem. C*, 2013, **117**, 11584−11591.

[3] G.X. Song, F. Xin, J.S. Chen, X.H. Yin, *Appl. Catal. A*, 2014, **473**, 90−95.

[4] J.H.Yang, D.G. Wang, H.X. Han, C. Li, *Acc. Chem. Res.*, 2013, **46**, 1900−1909.

[5] L.P. Wu, Y.L. Zhang, X.J. Li, C.P. Cen, *Phys. Chem. Chem. Phys.*, 2014, **16**, 15339−15345.

[6] Y. Hu, X. Gao, L. Yu, Y. Wang, J. Ning, S. Xu, X. W. Lou, *Angew. Chem. Int. Ed.*, 2013, **52**, 5636−5639.

[7] J. Xian, D. Li, J. Chen, X. Li, M. He, Y. Shao, L. Yu, J. Fang, *ACS Appl. Mater. Inter.*, 2014, **6**, 13157−13166.

[8] D. Meissner, C. Benndorf, R. Memming, *Appl. Surf. Sci.*, 1987, **27**, 423−436.

[9] K. M. G. Mostofa, C. Q. Liu, in K. M. G. Mostofa, T. Yoshioka, A. Mottaleb, D. Vione (Eds), Photobiogeochemistry of Organic Matter, Springer-Verlag Berlin Heidelberg, 2013, pp. 209−272.

[10] J. J. Yan, K. Wang, H. Xu, J. Qian, W. Liu, X. W. Yang, H. M. Li, *Chinese J. Catal.*, 2013, **34**,1876−1882.

[11] Y. H. Zhang, Z. Chen, S. Q. Liu, Y. J. Xu, *Appl. Catal. B*, 2013, **140−141**, 598−607.

[12] R. Lin, L. J. Shen, Z. Y. Ren, W. M. Wu, Y. Tan, H. Fu, J. Zhang, L. Wu, *Chem. Commun.*, 2014, **50**, 8533−8535.

[13] Y.J. Huang, W.C. Lo, S.W. Liu, C.H. Cheng, C.T. Chen, J.K. Wang, *Sol. Energ.*

Mat. Sol. C., 2013,**116**, 153−170.

[14] D. Jassby, J. F. Budarz, M. Wiesner, *Environ. Sci. Technol.*, 2012, **46**, 6934–6941.

[15] D. Lang, Q. Xiang, G. Qiu, X. Feng, F. Liu, *Dalton T.*, 2014, **43**, 7245–7253.

[16] H. Zhang, X. Lv, Y. M. Li, Y. Wang, J. H. Li, *ACS nano*, 2010, **4**, 380–386.

[17] P. Wang, T. Jiang, C. Zhu, Y. Zhai, D. Wang, S.J. Dong, *Nano Res.*, 2010, **3**, 794−799.

[18] A. Cao, Z. Liu, S. Chu, M. Wu, Z. Ye, Z. Cai, Y. Chang, S. Wang, Q. Gong, Y. Liu, *Adv. Mater.*, 2010, **22**, 103−106.

[19] C. B. Liu, Y. Teng, R. Liu, S. L. Luo, Y. H. Tang, L. Chen, Q. Cai, *Carbon*, 2011, **49**, 5312−5320.

[20] P. Gao, D. D. Sun, W. Ng, *J. Hazard. Mater.*, 2013, **250**−**251**, 412−420.

[21] I.V. Lightcap, T.H. Kosel, P.V. Kamat, *Nano Lett.*, 2010, **10**, 577−583.

[22] X. Zhao, S. Zhou, Q. Shen, L. P. Jiang, J. J. Zhu, *Analyst*, 2012, **137**, 3697−3703.

[23] R. Peng, C.M.. Wu, J. Baltrusaitis, N. M. Dimitrijevic, T. Rajh, R.T. Koodali, *Chem. Commun.*, 2013, **49**, 3221−3223.

[24] F. I. Hai, K. Yamamoto, K. Fukushi, *Crit. Rev. Env. Sci. Tec.*, 2007, **37**, 315–377.

[25] Y.H. Tang, S. L. Luo, Y. R. Teng, C. B. Liu, X. L. Xu, X. L. Zhang, L. Chen, *J.*

Hazard. Mater., 2012, **241**–**242**, 323– 330.

[26] G. Liu, P. Niu, L. Yin, H. M. Cheng, *J. Am. Chem. Soc.*, 2012, **134**, 9070−9073.

[27] D. J. Fermín, E.A. Ponomarev, L.M. Peter, *J. Electroanal. Chem.*, 1999, **473**, 192−203.

[28] A. K. Geim, K. S. Novoselov, *Nat. Mater.*, 2007, **6**, 183−191.

[29] A. G. Güell, N.Ebejer, M. E. Snowden, J. V. Macpherson, P. R. Unwin, *J. Am. Chem. Soc.*, 2012, **134**, 7258−7261.

[30] A. Iwase, Y. Hau Ng, Y. Ishiguro, A. Kudo, R. Amal, *J. Am. Chem. Soc.*, 2011, **133**, 11054−11057.

Captions and legends for Figures and Schemes

Fig. 1. SEM images of: (a) bare TiO_2 NT, (b) CdS–TiO_2 NT, (c) RGO–TiO_2 NT, (d) RGO/$CdS_{(5)}$–TiO_2 NT, (e) RGO/$CdS_{(7)}$–TiO_2 NT, and (f) RGO/$CdS_{(10)}$–TiO_2 NT. (g) TEM image of RGO/$CdS_{(5)}$–TiO_2 NT and (h) EDX of RGO/$CdS_{(5)}$–TiO_2 NT.

Fig. 2. Photocurrent responses of RGO/CdS–TiO_2 NT photocatalysts from different deposition cycles under UV-vis irradiation.

Fig. 3. XRD pattern of bare TiO_2 NT, CdS–TiO_2 NT and RGO/CdS–TiO_2 NT (A) and TPO profiles of CdS (1), CdS–TiO_2 NT (2), and RGO/CdS–TiO_2 NT (3) (B).

Fig. 4. Full XPS spectra (A); high resolution XPS spectra of S 2p (B) and Cd 3d (C): pure CdS (a), CdS–TiO_2 NT (b) and RGO/CdS–TiO_2 NT (c); high resolution XPS spectrum of C 1s (D): GO (a), RGO–TiO_2 NT (b) and RGO/CdS–TiO_2 NT (c).

Fig. 5. Diffuse reflectance UV-vis spectra of the photocatalysts under UV-vis irradiation (A) and their photocurrent responses (B).

Fig. 6. Adsorption of MB over different photocatalysts (The initial concentration of MB is 1 $mg.L^{-1}$) (A), photocatalytic degradation of MB over different photocatalysts under visible light irradiation (B), corresponding variation of $\ln(C_0/C)$ with MB degradation time (C), and photocatalytic stability of the photocatalysts on MB photocatalytic removal under visible-light irradiation (D).

Fig. 7. Photocatalytic degradation of PNP (A) or 2,4-D (B) over RGO/CdS–TiO_2 NT under visible light irradiation and the inset curves are the corresponding UV-vis absorbance variation of PNP or 2,4-D with degradation time.

Fig. 8. Time-dependent fluorescence emission of TAOH formed by the reaction of TA with •OH radicals generated by the photocatalysts under visible-light irradiation.

Fig. 9. SEM images of CdS–TiO_2 NT (a1-4) and RGO/CdS–TiO_2 NT (b1-4) after 2000-min visible light irradiation: in the presence of EDTA-2Na and N_2 (a1 and b1), in the presence of only EDTA-2Na (a2 and b2), in the presence of only *t*BuOH (a3 and b3), and in the absence of scavenger and N_2 (a4 and b4). The corresponding curves of irradiation time-dependent Cd concentration in solution on CdS–TiO_2 NT (Black line) and RGO/CdS–TiO_2 NT (Red line) (c1-c4).

Scheme 1. Scheme of RGO/CdS–TiO_2 NT structure.

Scheme 2. Photocatalytic mechanism of RGO/CdS–TiO_2 NT.

Scheme 3. Schematic diagram of photocorrosion inhibition mechanism.

Fig. 1

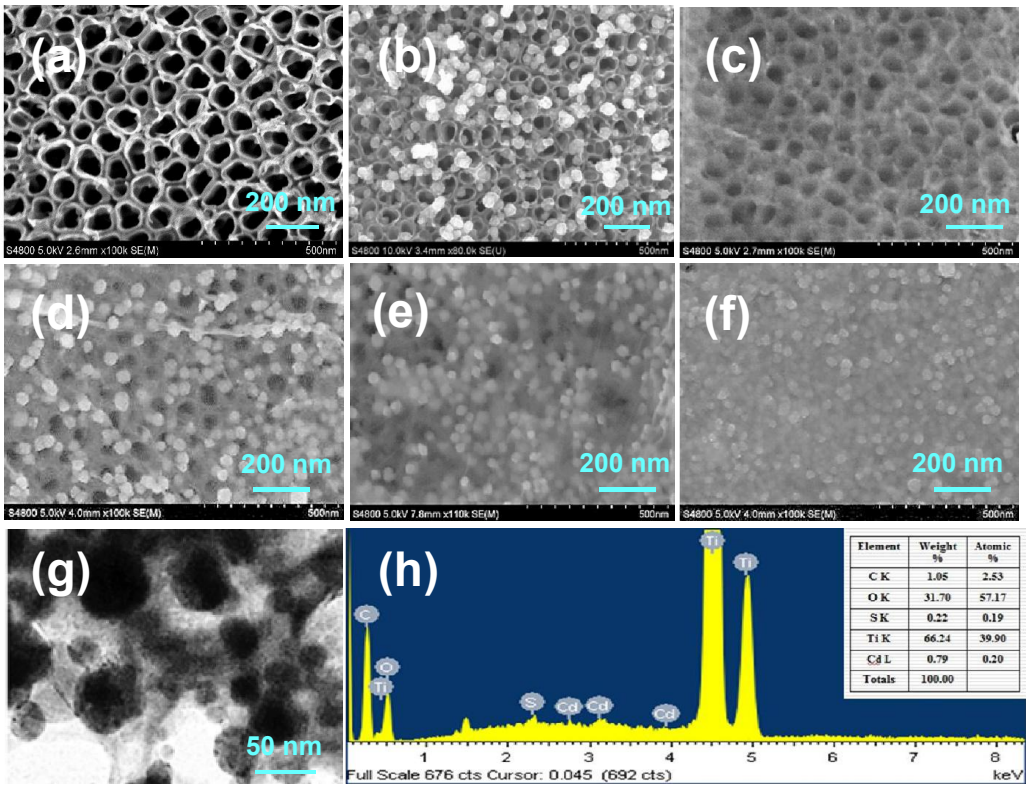

Fig. 2

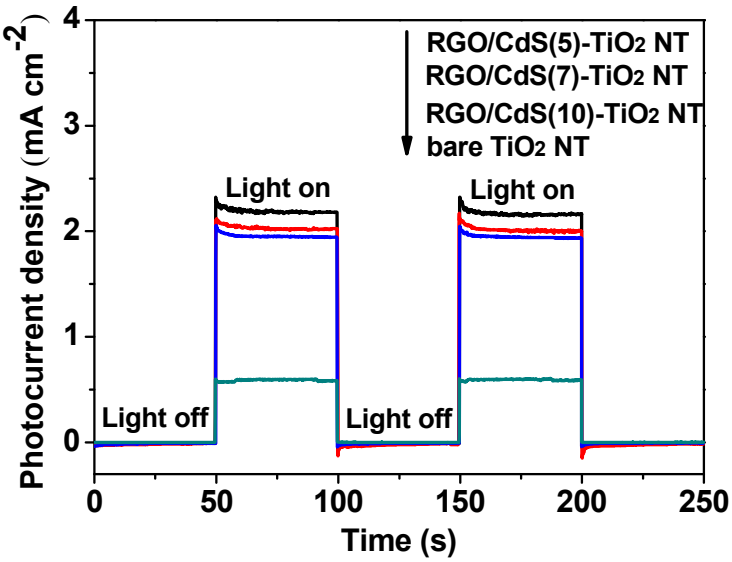

Fig. 3

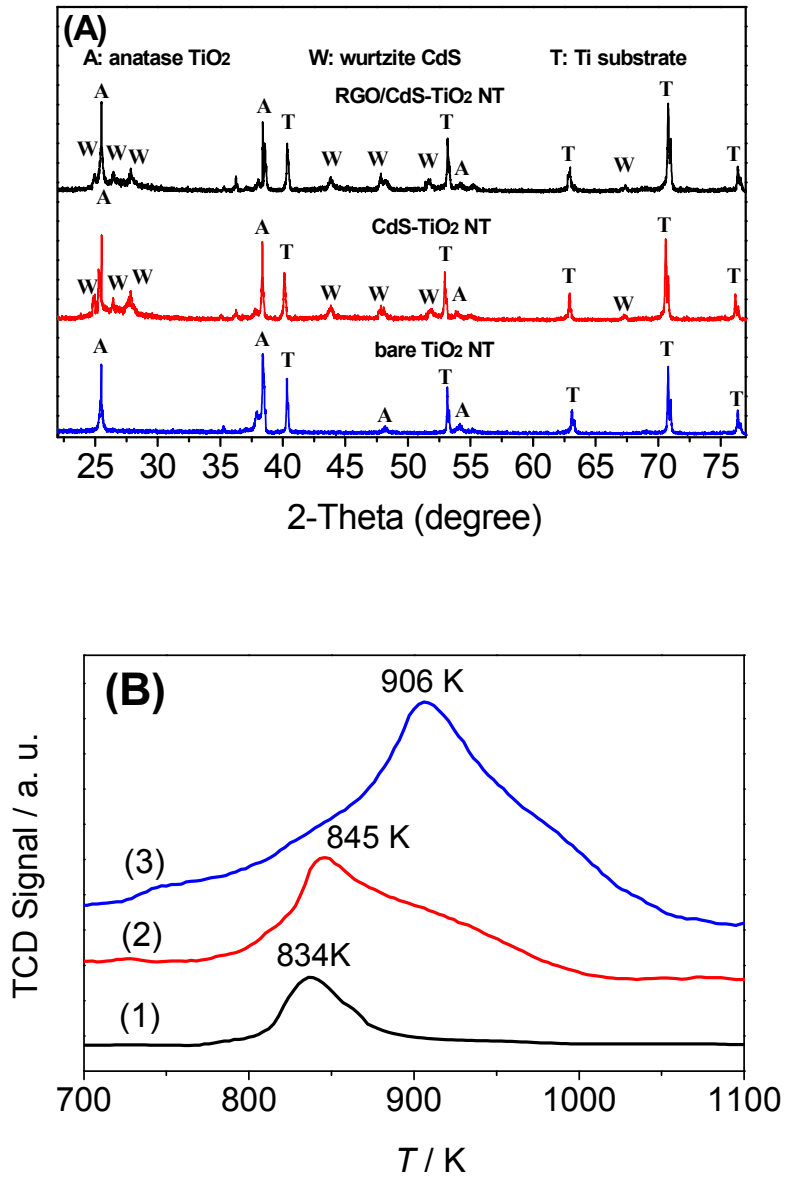

Fig. 4

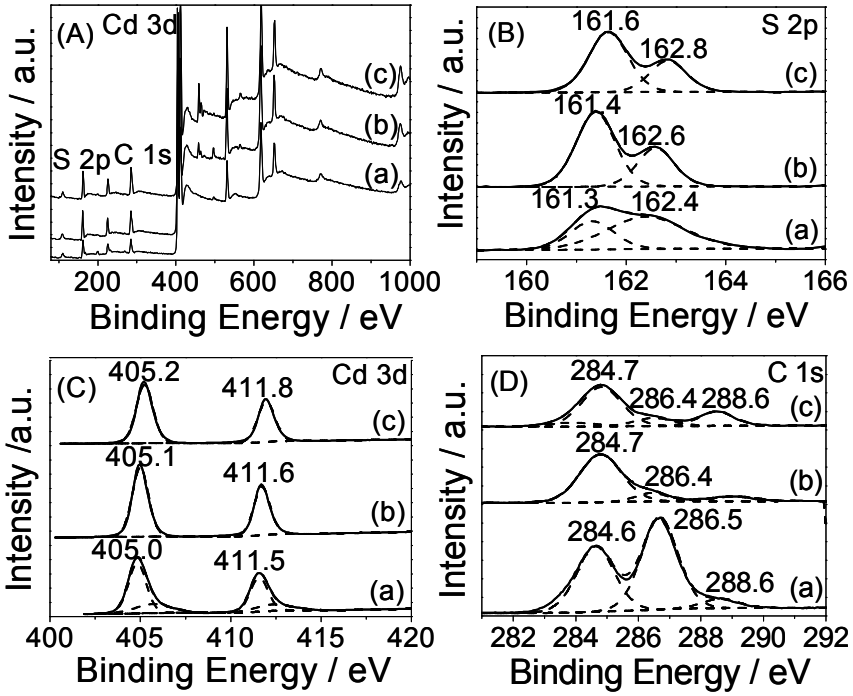

Fig. 5

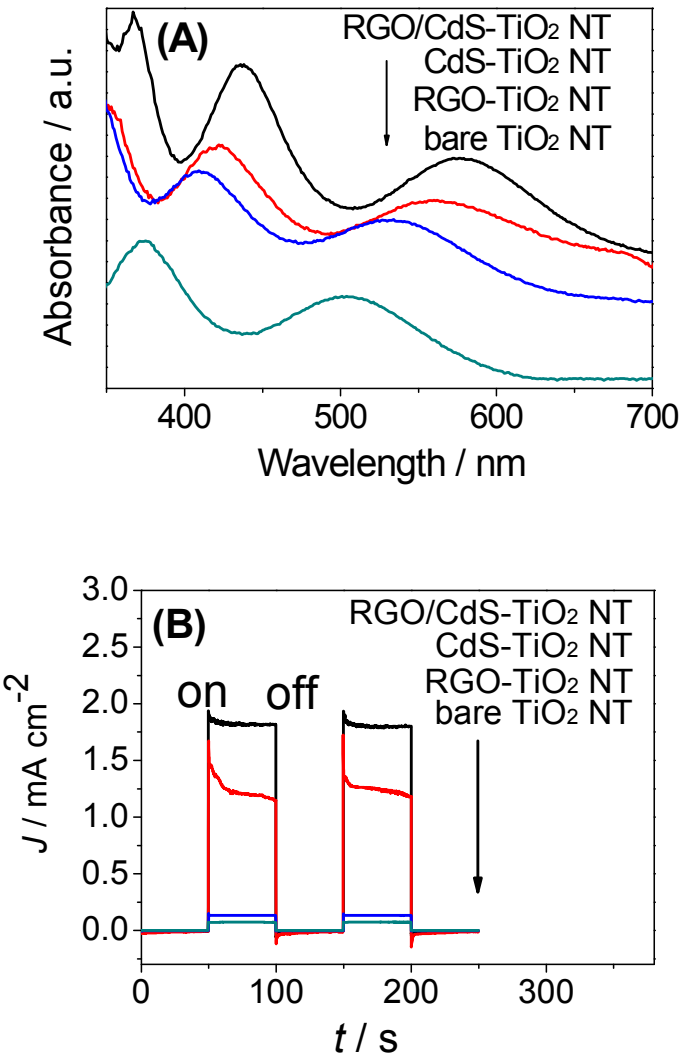

Fig. 6

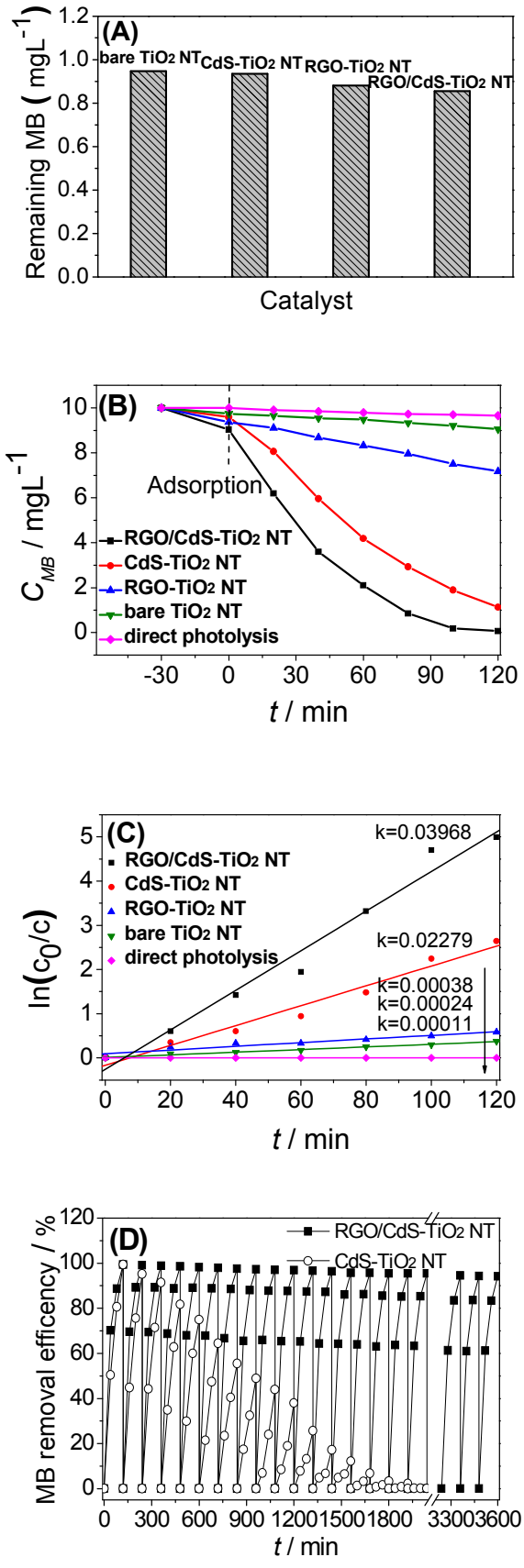

Fig. 7

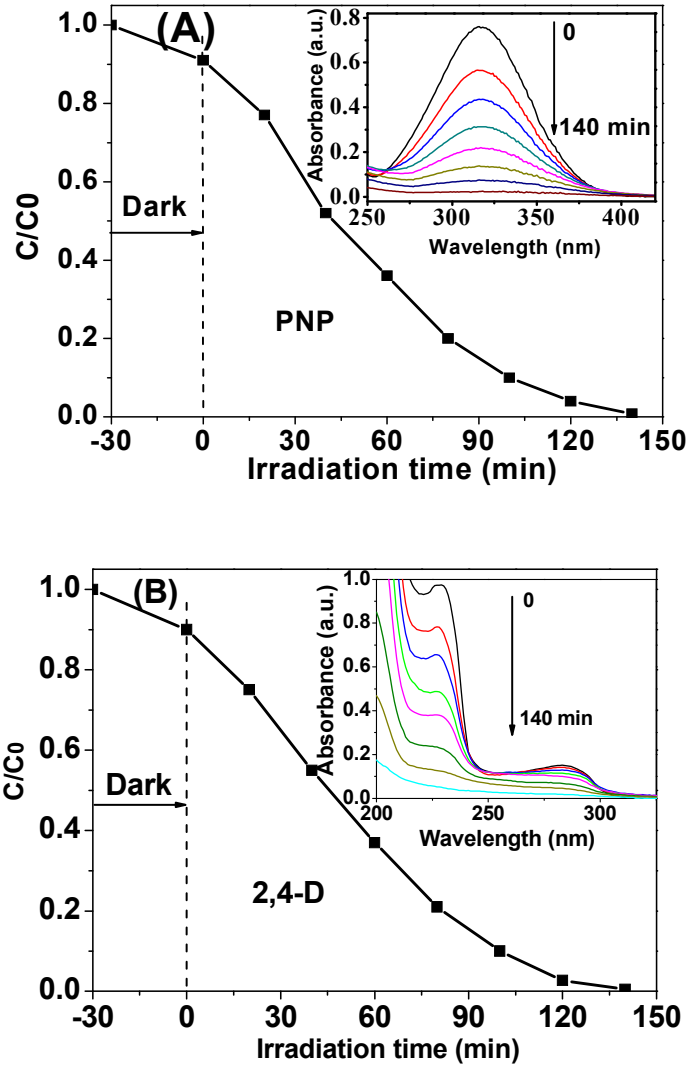

Fig. 8

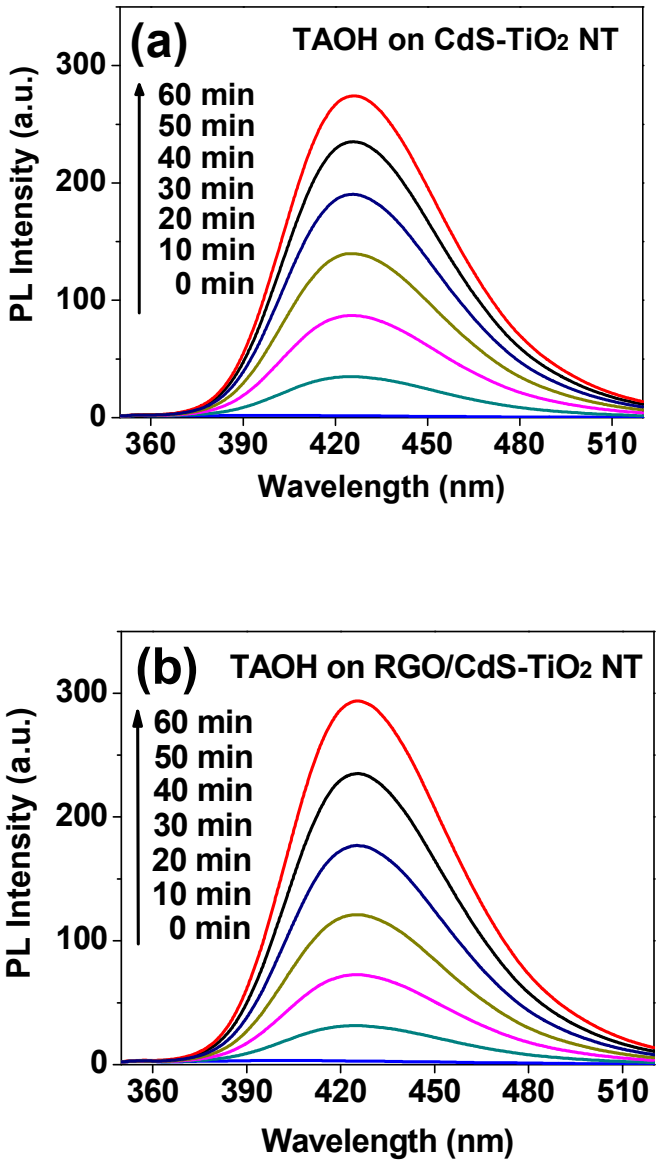

Fig. 9

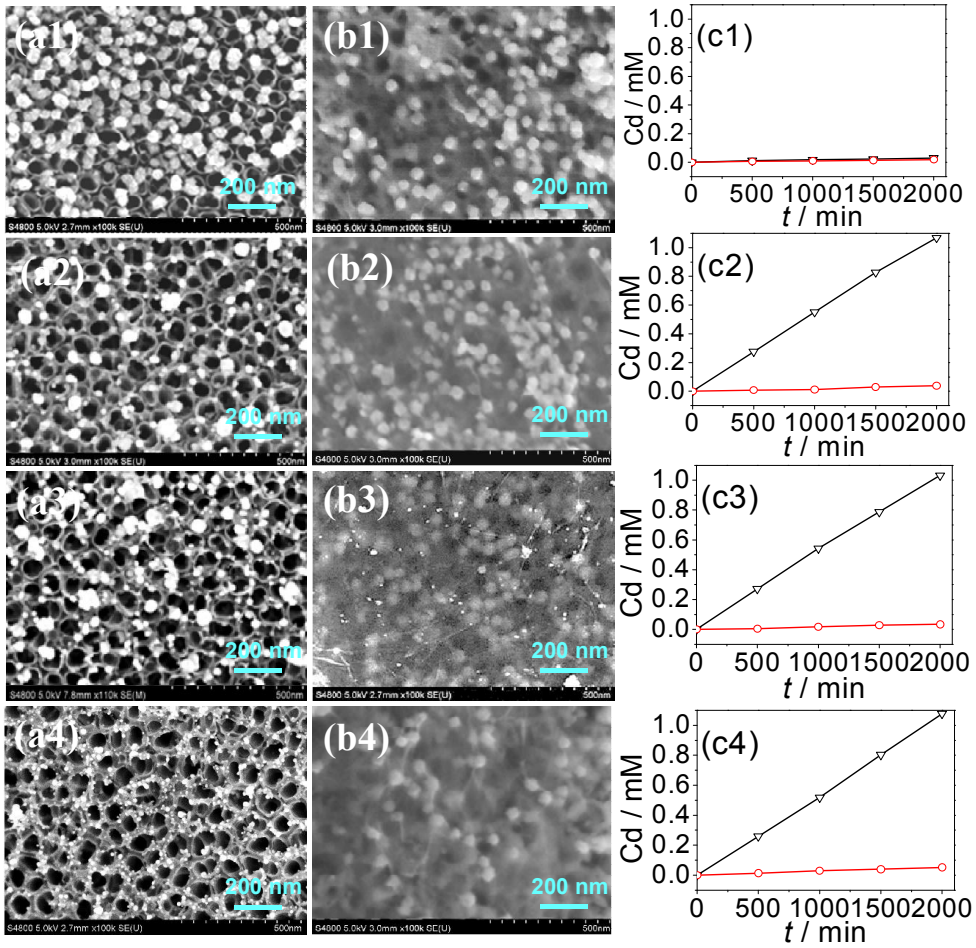

Scheme 1

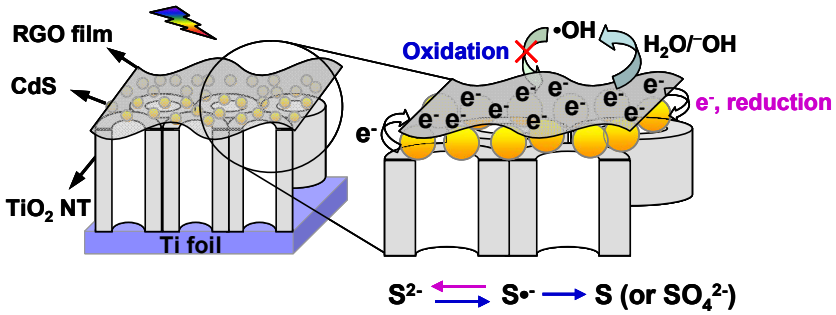

Scheme 2

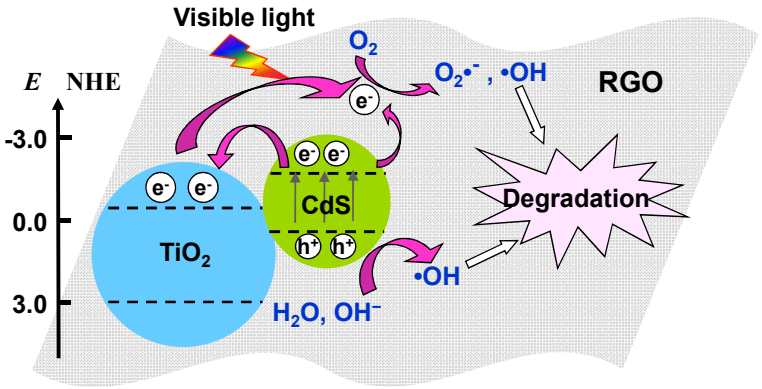

Scheme 3